

## ARTICLE

## OPEN

# Sea ice and atmospheric circulation shape the high-latitude lapse rate feedback

Nicole Feldl  <sup>1</sup>✉, Stephen Po-Chedley  <sup>2</sup>, Hansi K. A. Singh  <sup>3</sup>, Stephanie Hay <sup>4</sup> and Paul J. Kushner <sup>4</sup>

Arctic amplification of anthropogenic climate change is widely attributed to the sea-ice albedo feedback, with its attendant increase in absorbed solar radiation, and to the effect of the vertical structure of atmospheric warming on Earth's outgoing longwave radiation. The latter lapse rate feedback is subject, at high latitudes, to a myriad of local and remote influences whose relative contributions remain unquantified. The distinct controls on the high-latitude lapse rate feedback are here partitioned into "upper" and "lower" contributions originating above and below a characteristic climatological isentropic surface that separates the high-latitude lower troposphere from the rest of the atmosphere. This decomposition clarifies how the positive high-latitude lapse rate feedback over polar oceans arises primarily as an atmospheric response to local sea ice loss and is reduced in subpolar latitudes by an increase in poleward atmospheric energy transport. The separation of the locally driven component of the high-latitude lapse rate feedback further reveals how it and the sea-ice albedo feedback together dominate Arctic amplification as a coupled mechanism operating across the seasonal cycle.

*npj Climate and Atmospheric Science* (2020)3:41; <https://doi.org/10.1038/s41612-020-00146-7>



## INTRODUCTION

In climate simulations forced by increasing concentrations of atmospheric CO<sub>2</sub>, changes in the rate at which temperature decreases with altitude (i.e., changes in the lapse rate) act as an important negative feedback in the global climate system<sup>1–3</sup>. The lapse rate feedback, defined as the radiative feedback associated with atmospheric warming that is vertically nonuniform, is negative at low latitudes. This negative feedback arises because moist convection leads to greater warming in the upper than in the lower troposphere, which increases outgoing longwave radiation and thus counteracts further surface warming. The resulting negative tropical lapse rate feedback determines the negative sign of the global lapse rate feedback. However, the lapse rate feedback is also influenced by regions in which the lower troposphere exhibits greater warming than the upper troposphere, leading to a smaller increase in outgoing longwave radiation relative to uniform warming and hence a positive feedback. Bottom-heavy warming occurs in the polar atmosphere where stable stratification inhibits vertical mixing and traps warming near the surface<sup>4,5</sup>. The distinct, competing tropical and high-latitude processes that shape the meridional structure of the lapse rate feedback have been recognized as major contributors to polar-amplified surface warming<sup>6–9</sup>.

Surface-amplified warming over the Arctic Ocean is controlled by the changing seasonal dynamics of sea ice. Climatological sea ice retreat during summer increases absorbed solar radiation and warms the ocean mixed layer. In the fall, the atmosphere cools rapidly, increasing the air-sea temperature gradient; the resulting increase in upward turbulent heat fluxes cools the ocean surface and warms and moistens the atmosphere. In a warming climate, sea ice loss is characterized by enhanced summer melt<sup>10–12</sup> and, correspondingly, enhanced winter lower-tropospheric warming<sup>13–15</sup>. The causal link between sea ice loss and surface-amplified wintertime warming has been confirmed in climate model experiments in which the sea ice

component of a coupled ocean-atmosphere model is perturbed in isolation from other confounding factors<sup>16–21</sup>.

In addition to the local impact of sea ice changes on the thermal structure of the atmosphere, poleward energy transport in the atmosphere provides a remote influence on the local lapse rate. In a warming climate, the advection of warm air poleward and upward warms the upper troposphere<sup>22–24</sup>. This process, remotely driven by low-latitude warming, results in a weakened lapse rate feedback in high latitudes for models with large increases in atmospheric heat transport<sup>25–27</sup>. Low-latitude warming has been shown to drive, in particular, an increase in poleward latent heat transport, which additionally affects Arctic water vapor and cloud feedbacks<sup>28</sup>. The high-latitude lapse rate feedback is also reduced by targeted remote forcings, such as a CO<sub>2</sub> forcing applied strictly to the midlatitudes<sup>29</sup> or an idealized, purely advective forcing<sup>9,30</sup>.

The local and remote controls identified in prior work are highlighted when we perform a model experiment in which a sea-ice albedo perturbation is compared to a greenhouse-gas forcing (Fig. 1). In these simulations, the Arctic lapse rate feedback is more positive under sea-ice albedo reduction than under greenhouse gas increase (Fig. 1a, b). A pattern-scaling decomposition of the atmospheric temperature response into parts associated with low-latitude warming and with the local response to sea ice loss (see "Methods")<sup>20,31</sup> suggests that this difference is not a mere artifact of the albedo-reduction protocol, revealing distinct patterns of the lapse rate feedback (Fig. 1c, d). In particular, low-latitude warming drives, in the high latitudes, a modest positive feedback over continents and a modest negative feedback over oceans. However, it is the atmospheric warming associated with sea ice loss that produces a positive lapse rate feedback over the Arctic Ocean and amplifies surface warming.

Motivated by this perspective and by the numerous studies highlighting various controls on the polar lapse rate, we seek to

<sup>1</sup>Department of Earth and Planetary Sciences, University of California, Santa Cruz, CA, USA. <sup>2</sup>Program for Climate Model Diagnosis and Intercomparison (PCMDI), Lawrence Livermore National Laboratory, Livermore, CA, USA. <sup>3</sup>School of Earth and Ocean Sciences, University of Victoria, Victoria, BC, Canada. <sup>4</sup>Department of Physics, University of Toronto, Toronto, ON, Canada. email: nfeldl@ucsc.edu

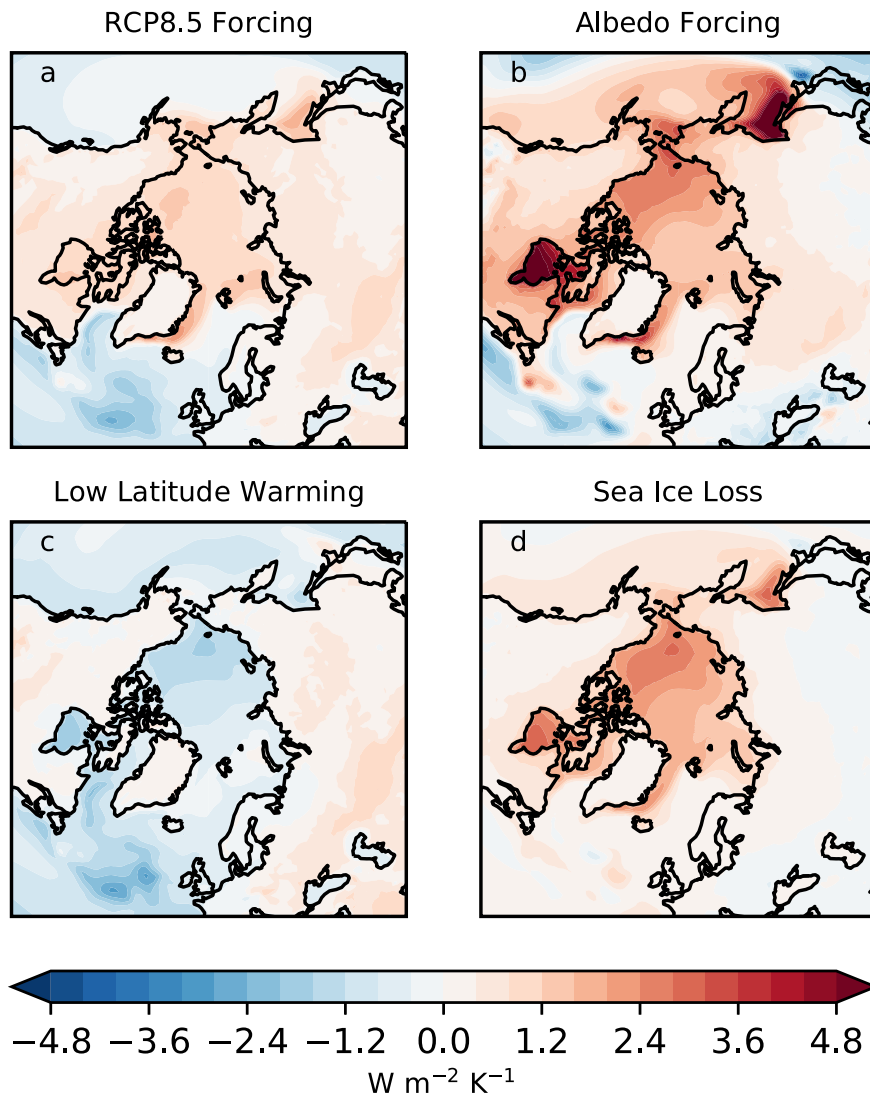


**Fig. 1 Lapse rate feedback for different forcings and contributions to the forced response in CESM.** **a** The annual-mean lapse rate feedback for the ensemble-mean response to RCP8.5 forcing, expressed as the difference between the 2027–2036 epoch and the 2057–2066 epoch. **b** As in **a**, but for the response to sea-ice albedo forcing, expressed as the difference between the multi-centennial mean of the sea-ice albedo perturbation integration and the multi-centennial quasi-equilibrated mean of a constant year 2000 radiative forcing integration. **c** The annual-mean lapse rate feedback for low-latitude surface warming. **d** As in **c**, but for the response to sea ice loss. The feedbacks for the partial responses, **c** and **d**, sum to **a**.

separate the local and remote components of the high-latitude lapse rate feedback. We introduce a simple, explicit decomposition of the lapse rate feedback into contributions arising from dynamically distinct atmospheric regions. We then show how this decomposition separates surface-based mechanisms such as sea ice retreat that contribute positively to lapse rate feedback from negative contributions associated with tropical convection and advective atmospheric energy transport. Furthermore, this decomposition facilitates examination of statistical relationships across current climate models, which, we contend, deepens our theoretical understanding of the lapse rate feedback in nature.

## RESULTS

Partitioning local and remote influences on the high-latitude lapse rate feedback

The 285-K isentrope is selected as the basis for our diagnosis of upper and lower lapse rate feedbacks from the CMIP5

abrupt4xCO<sub>2</sub> and piControl simulations. The upper lapse rate feedback accounts for deviations in atmospheric warming relative to temperature changes that occur on the climatological 285-K surface. In contrast, the lower lapse rate feedback accounts for deviations in atmospheric warming relative to surface temperature change. The radiative impact of these temperature changes is calculated using radiative kernels. The lower lapse rate feedback is comprised of contributions from the surface to the 285-K isentrope and the upper lapse rate feedback of contributions from the 285-K isentrope to the tropopause (see “Methods”).

Since the 285-K isentrope intersects the Earth’s surface in the midlatitudes, it effectively isolates the high-latitude lower-tropospheric warming from both higher altitudes and lower latitudes. It also allows for convective coupling in the tropics between the surface and upper troposphere; in this region the lower lapse rate feedback is zero by construction. Previous work has demonstrated, in single models, an enhancement of the high-latitude lapse rate feedback by the surface albedo feedback<sup>8,32</sup>, or, equivalently, an enhancement of the surface-intensified warming by sea ice loss<sup>15–21</sup>. Instead of artificially intervening in feedback processes in

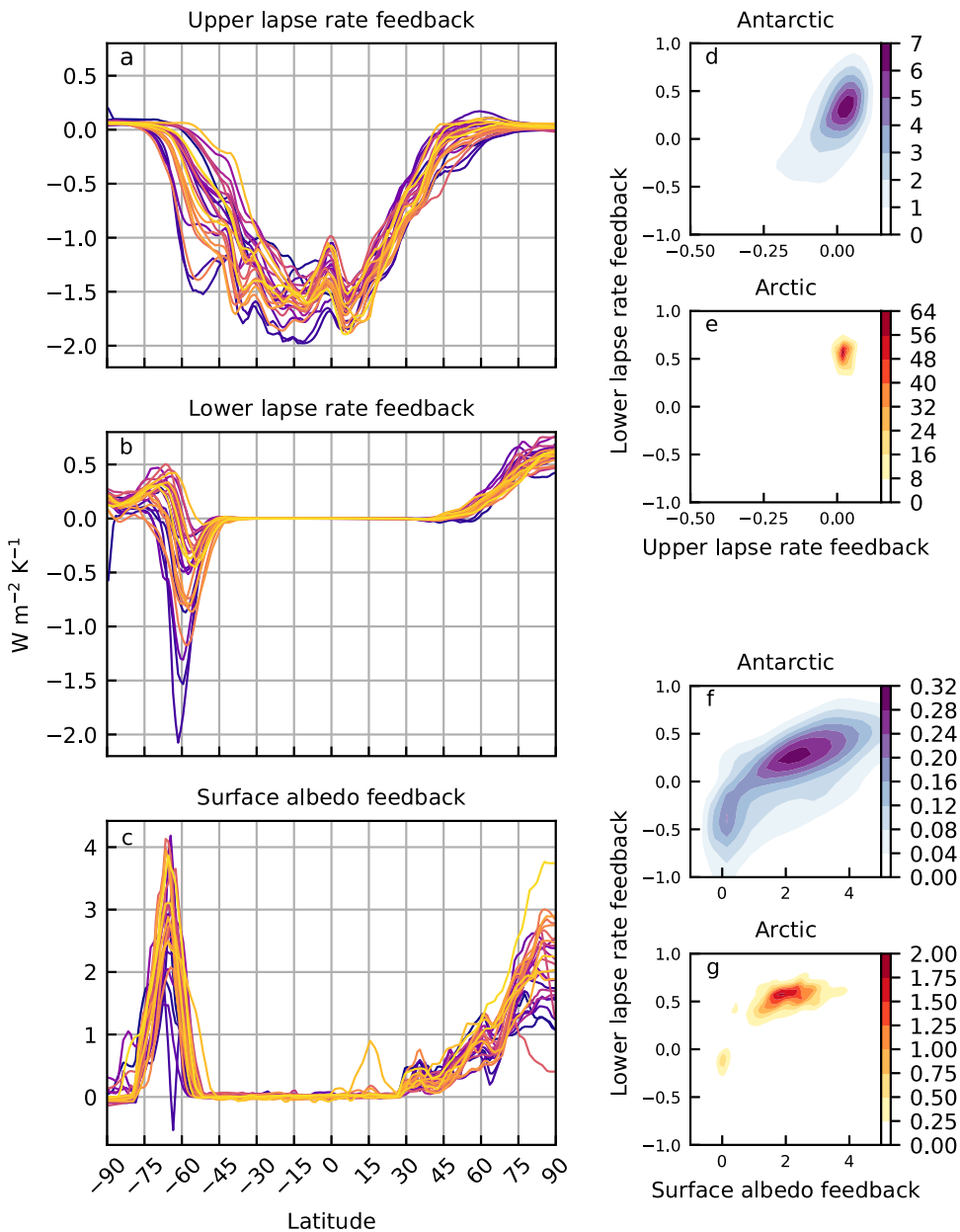


**Fig. 2 Decomposition of radiative feedbacks in CMIP5.** **a** The upper lapse rate feedback associated with warming of low latitudes (all levels) and high latitudes aloft, **b** the lower lapse rate feedback associated with high-latitude lower-tropospheric warming, and **c** the surface albedo feedback. A probability density function (PDF) of the local lower lapse rate feedback and the local upper lapse rate feedback for the composite of all models and all grid cells poleward of **d** 60S and **e** 60N in units  $\text{W m}^{-2} \text{K}^{-1}$  for an ocean-only domain. A PDF of the local lower lapse rate feedback and the local surface albedo feedback for all models and all grid cells poleward of **f** 60S and **g** 60N in units  $\text{W m}^{-2} \text{K}^{-1}$  for an ocean-only domain.

individual models, our decomposition exploits the regionality of the physical processes contributing to the lapse rate feedback. This allows a diagnosis of the relative importance and robustness of these contributions across the free-running coupled climate model ensemble.

The diagnosed upper and lower lapse rate feedbacks are consistent in sign with the conventional lapse rate feedback and its global mean. The upper lapse rate feedback is broadly negative, maximizing in magnitude in the tropics where warming is greatest aloft (Fig. 2a). However, as expected, moist adiabatic warming is insufficient to explain the lapse rate feedback at high latitudes, where the lower lapse rate feedback makes substantial contributions (Fig. 2b). In particular, the lower lapse rate feedback is positive in the Arctic where there is snow and ice melt

associated with a positive surface albedo feedback (Fig. 2c). It tends to be negative over the Southern Ocean where large-scale ocean upwelling reduces surface warming<sup>33</sup> and decouples the surface from the tropospheric response<sup>27,34</sup>. Hence, both the upper and lower lapse rate feedback contribute to the negative feedback—and large intermodel variability—over the Southern Ocean. The upper lapse rate feedback also exhibits considerable model spread in the northern subpolar regions, though it falls consistently to zero at the pole.

We evaluate the statistical relationships between the upper and lower lapse rate feedback and between the lower lapse rate feedback and surface albedo feedback for each polar region separately (Fig. 2d–g). Significant Pearson correlations are present in all regions at the 95% level. Notably, in the southern

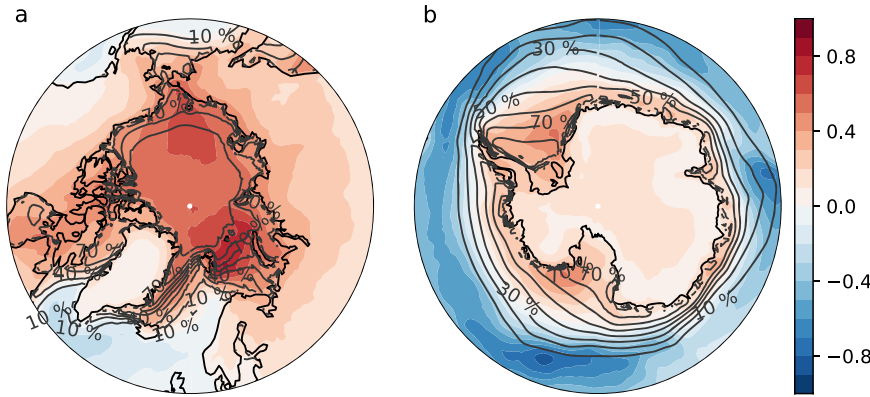


**Fig. 3 Multimodel-mean lower lapse rate feedback and climatological sea ice concentration for the polar regions.** Color shading represents the annual-mean lower lapse rate feedback ( $\text{W m}^{-2} \text{K}^{-1}$ ) for the **a** the Arctic and **b** the Antarctic. Contour lines (10% interval) indicate climatological annual-mean sea ice concentration.

hemisphere, a more negative lower lapse rate feedback is associated with a more negative upper lapse rate feedback ( $r = 0.69$ ). It is apparent from Fig. 2a, b that the source of the positive correlation is the Southern Ocean, a complex region of suppressed surface warming and moderate atmospheric warming. Additionally, both hemispheres exhibit positive correlations between the lower lapse rate feedback and the surface albedo feedback ( $r = 0.59$ ). Figure 2f–g shows that a more positive lower lapse rate feedback is associated with a larger surface albedo feedback, suggesting the physical processes are not independent.

#### The two feedbacks of sea ice retreat

By permitting the surface to be colder than the overlying air, the presence of sea ice preconditions a strongly positive lapse rate feedback over ocean regions. This relationship is evident in the Arctic, where the transition from a negative to positive lower lapse rate feedback closely follows the 10% annual-mean sea ice concentration, both for individual models (Fig. S1) and the multimodel mean (Fig. 3a). The Arctic-average multimodel-mean lower lapse rate feedback is  $0.34 \text{ W m}^{-2} \text{K}^{-1}$ , and the dominant contribution is from sea ice regions (69.5%) (land and open ocean contribute 31.3% and  $-0.8\%$ , respectively). In the Antarctic, the lower lapse rate feedback tends to track the 10% sea ice contour for most models (Fig. S2); however, the correspondence is weaker in the multimodel mean (Fig. 3b), consistent with the large intermodel variability. Hence, for the lower lapse rate feedback, we focus the following results on the Arctic.

The relationship between the lower lapse rate feedback and sea ice change is further investigated via local, intermodel correlations over an ocean-only domain. In particular, we are interested in the impact of Arctic sea ice retreat during summer (when the shortwave surface albedo feedback maximizes) on the boundary layer during winter (when the longwave lapse rate feedback maximizes)<sup>35,36</sup>. Models with a larger reduction in summertime sea ice exhibit a more positive lower lapse rate feedback (Fig. 4a). That relationship is explicated through the following seasonal atmosphere–ocean–cryosphere interactions. First, models with larger decreases in summer sea ice concentration have larger decreases in late fall/early winter sea ice concentration (Fig. 4b). Second, in fall/winter, larger decreases in sea ice concentration are associated across models with larger increases in surface sensible and latent heat flux (Fig. 4c) and larger decreases in the temperature inversion (calculated as the difference between temperature at 850 hPa and surface air temperature; Fig. 4d). Finally, larger decreases in the inversion necessitates a more positive lower lapse rate feedback (Fig. 4e), leading to further warming. Notably, these relationships are spatially robust; broadly throughout the Arctic, models with

greater sea ice loss produce a greater weakening of the temperature inversion and a more positive lapse rate feedback.

This delayed impact of summer sea ice loss is consistent with prior work<sup>13–15</sup>. Decreased summer sea ice permits greater heating of the underlying oceanic mixed layer, and warm anomalies persist into the following fall and winter when the mixed layer cools to its freezing temperature through radiative and turbulent surface processes. Further evidence that the atmospheric warming over the Arctic Ocean is primarily due to surface processes is provided by the heating rate responses for the simulations presented in Fig. 1. It is apparent from the magnitude and structure of the responses that the dominant contribution in ocean regions is vertical diffusion of upward surface turbulent heat flux anomalies (Fig. S3). Additional, albeit much smaller, warming in the upper part of the boundary layer is due to condensational heating (attributed by refs. <sup>37,38</sup> to moisture sourced through increased local evaporation), while contributions to the heat budget by longwave radiation are small.

#### Remote influence of atmospheric heat transport

To evaluate the remote influence on the upper lapse rate feedback, we calculate the change in atmospheric energy transport (AET) between the CMIP5 abrupt4xCO<sub>2</sub> and piControl simulations. Under CO<sub>2</sub> quadrupling, poleward AET increases in the low- to midlatitudes by up to approximately 0.1–0.15 PW per degree global-mean surface warming and, in the northern hemisphere, decreases in the high latitudes (Fig. 5a). Models are color-coded by the magnitude of the upper lapse rate feedback averaged poleward of 50° latitude. The choice of this averaging area was physically motivated by the structure of the upper lapse rate feedback (Fig. 2a) to include subpolar regions where the feedback exhibits high intermodel variability. In both hemispheres, the change in poleward energy transport at 50° latitude is negatively correlated with the high-latitude upper lapse rate feedback. By warming the high-latitude upper troposphere, atmospheric energy transport promotes a negative upper lapse rate feedback, and this holds across models. Equivalently, models with a decrease in poleward energy transport tend to have a less negative upper lapse rate feedback. Linear regression reveals that the high-latitude upper lapse rate feedback varies across models by  $-1.5 \text{ W m}^{-2} \text{K}^{-1}$  per PW K<sup>-1</sup> in the northern hemisphere—in other words, a 0.1 PW K<sup>-1</sup> increase in transport at 50°N is associated with a  $0.15 \text{ W m}^{-2} \text{K}^{-1}$  reduction in the Arctic upper lapse rate feedback. At 60° latitude, statistical relationships remain significant but are weaker (Fig. S4), consistent with the diminishing upper lapse rate feedback in polar regions and its particular importance for subpolar regions (Fig. 2a).

A partitioning of the atmospheric energy transport is performed to further reveal the relationship between the upper lapse rate

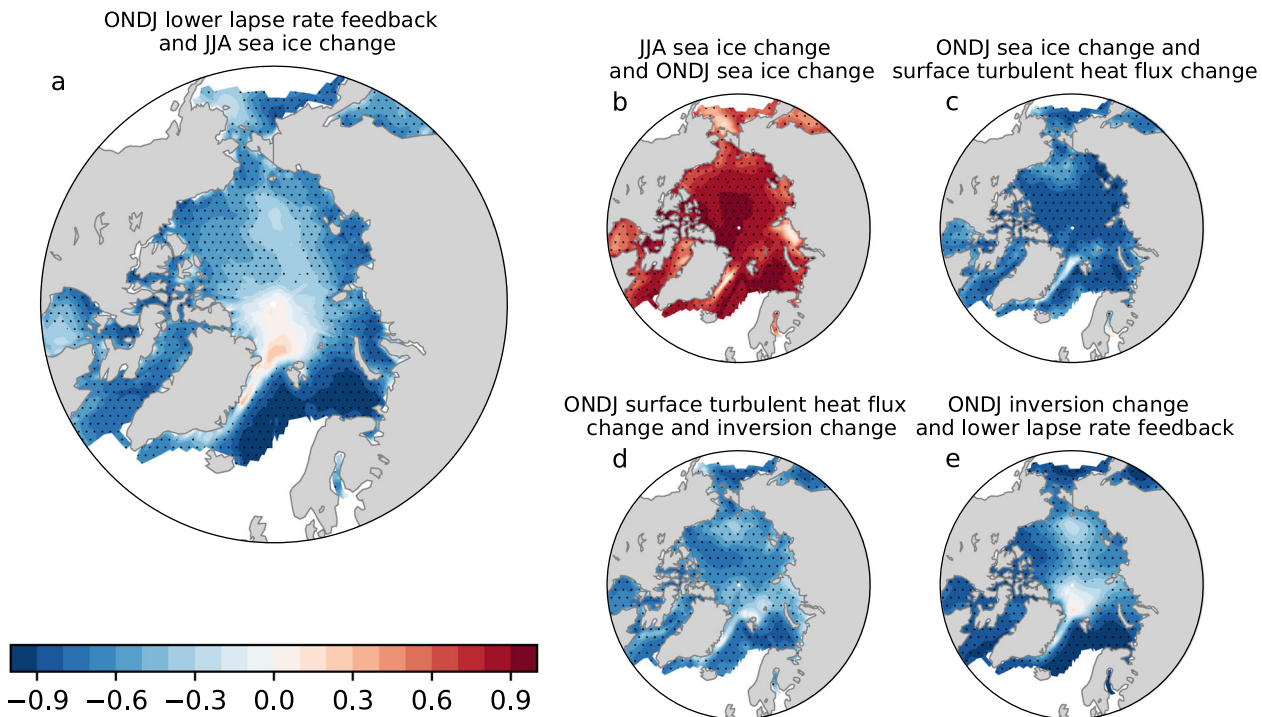


**Fig. 4 Map of Pearson correlation coefficient across models between winter lower lapse rate feedback and change in surface and boundary-layer properties in the Arctic.** Correlation coefficient between **a** early fall/late winter (ONDJ; October through January) lower lapse rate feedback and change in summer (JJA; June through August) sea ice concentration, **b** change in JJA sea ice concentration and change in ONDJ sea ice concentration, **c** change in ONDJ sea ice concentration and change in ONDJ surface turbulent heat flux, **d** change in ONDJ surface turbulent heat flux and change in ONDJ inversion strength, calculated as the difference between air temperature at 850 hPa and near-surface air temperature ( $T_{850} - T_s$ ), and **e** change in ONDJ inversion strength and ONDJ lower lapse rate feedback. Regions of multimodel-mean sea ice concentration <10% are masked to reduce spurious correlations. Stippling indicates correlations that are statistically significant at the 95% level.

feedback and circulation changes (Fig. 5). We focus first on the northern hemisphere. The transient eddy energy transport (Fig. 5b), and specifically its latent heat flux component (Fig. 5d), dominate the increase in total AET in the midlatitudes. Moreover, models with a larger increase in latent transient eddy energy transport (Fig. 5d) and a smaller decrease in the dry transient eddy energy transport (Fig. 5c) are both associated with a more negative upper lapse rate feedback. In other words, in any given model, changes in latent heat flux and dry static energy flux by transient eddies tend to oppose one another; however, across models, changes in these fluxes co-vary with the magnitude of the upper lapse rate feedback. This relationship between a more anomalous poleward energy transport and a more negative upper lapse rate feedback is qualitatively the same in the southern hemisphere, albeit with larger anomalies and higher correlations.

The mean meridional circulation exhibits relatively small changes in energy transport at high latitudes, though the increase in equatorward transport is correlated with the high-latitude upper lapse rate feedback (Fig. S5). We interpret this as indicating compensation between circulation components. No intermodel relationship is apparent between changes in energy transport by stationary eddies and the upper lapse rate feedback.

## DISCUSSION

To quantify the relative importance of the physical mechanisms known to shape the high-latitude lapse rate feedback, we have partitioned the effects of local surface processes and remote atmospheric energy transport. We have clarified how the positive lapse rate feedback over the Arctic Ocean is tied to sea ice retreat and furthermore represents the changing seasonal dynamics of sea ice. Specifically, the presence of sea ice enables a temperature

inversion, and summertime sea ice retreat leads to the erosion of the wintertime inversion via ocean–atmosphere heat exchange. The enhancement of these processes in a warmer world drives an increase in surface-amplified warming and hence a positive feedback. This mechanism is likely strongest for climates that have experienced substantial summer sea ice loss; however, any summer sea ice decline and ocean mixed layer heating will necessitate some degree of trapped boundary-layer warming in fall and winter as sea ice re-grows. Our results show that, *in the polar regions*, the lapse rate feedback is dominated by low-level warming. Across the multimodel ensemble, we have quantified the positive correlation between the lapse rate and albedo feedbacks, suggesting they amplify one another in a manner consistent with previous locked-albedo or albedo-reduction simulations<sup>8,32</sup>. Taken together, the lapse rate feedback and surface albedo feedback comprise a longwave and shortwave response to sea ice loss, respectively.

Statistical relationships across the multimodel ensemble quantify the degree to which a larger increase in poleward atmospheric energy transport is associated with a more negative upper lapse rate feedback, thus reducing the magnitude of the positive high-latitude lapse rate feedback. The increases in energy transport are attributed to relatively strong increases in the latent heat transport by transient eddies that are only partially compensated by weak decreases in the dry static energy transport. This transport effect dominates model spread in the lapse rate feedback *in subpolar regions*, possibly related to variability in patterns of tropical sea surface temperature change<sup>39,40</sup>, and by implication is important in determining the latitude at which the lapse rate feedback changes sign. While further work is needed to understand feedback partitioning in regions of strong ocean heat uptake, such as the Southern Ocean, these results demonstrate that

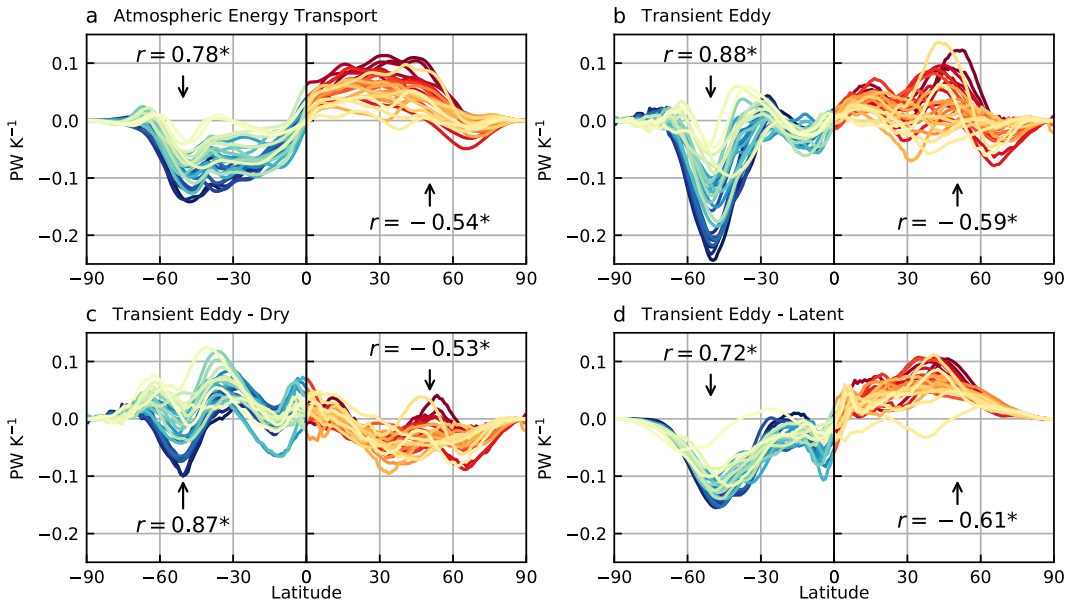


**Fig. 5 Change in northward atmospheric energy transport under  $\text{CO}_2$  quadrupling.** Change in **a** total atmospheric energy transport, **b** energy transport by transient eddies, and the **c** dry and **d** latent components of the transient eddy energy transport. All transports are normalized by the global-mean warming to give units of  $\text{PW K}^{-1}$ . Models are color-coded (separately for each hemisphere) by the magnitude of the upper lapse rate feedback averaged poleward of  $50^\circ\text{N/S}$  with red (blue) indicating a strong negative feedback in the northern (southern) high latitudes. The Pearson correlation coefficient between each transport at  $50^\circ$  and the upper lapse rate feedback averaged  $50\text{--}90^\circ$  is displayed on the plot for each hemisphere. Note that a positive correlation coefficient for *northward* transport in the southern hemisphere indicates a negative correlation coefficient for *poleward* transport. Asterisks indicate correlations that are statistically significant at the 95% level.

decomposing the lapse rate feedback into “upper” and “lower” atmospheric contributions is an important step towards untangling local and remote influences on the Arctic lapse rate feedback.

Feedbacks that are dynamically linked may be combined to assess their contributions to Arctic amplification of surface warming (Fig. 6). The combined water vapor and upper lapse rate feedbacks contribute neither to Arctic amplification nor to tropical amplification: they exhibit striking compensation, falling along the 1:1 line. This is consistent with the well-known compensation between global water vapor and lapse rate feedbacks<sup>3</sup>, but here we demonstrate the impact on the meridional structure of warming. In other words, greater warming and moistening of the upper troposphere does not produce Arctic amplification. Rather, the dominant contribution arises from the combined surface albedo and lower lapse rate feedbacks.

As a result of this work, we are able to establish that the high-latitude lapse rate feedback associated with a greenhouse-gas radiative forcing contributes to Arctic amplification through the same controlling factor as the surface albedo feedback, namely sea ice loss. Furthermore, it will be greatest in the case of extensive sea ice retreat combined with little increase in atmospheric energy transport for a given amount of global warming. We argue it is ambiguous to frame the lapse rate feedback as having greater importance than the surface albedo feedback to Arctic amplification, since both feedbacks are rooted in the same physical mechanism. Rather, they reflect a season-spanning pathway by which the high latitudes, particularly the Arctic, are uniquely sensitive to a changing climate.

## METHODS

### CMIP5 output

Monthly mean data from 27 models from phase 5 of the Coupled Model Intercomparison Project (CMIP5)<sup>41</sup> are used in this study: ACCESS1-0, ACCESS1-3, bcc-csm1-1-m, bcc-csm1-1, BNU-ESM, CanESM2, CCSM4,

CNRM-CM5, CSIRO-Mk3-6-0, FGOALS-g2, GFDL-CM3, GFDL-ESM2G, GFDL-ESM2M, GISS-E2-H, GISS-E2-R, HadGEM2-ES, inmcm4, IPSL-CM5A-LR, IPSL-CM5A-MR, IPSL-CM5B-LR, MIROC5, MIROC-ESM, MPI-ESM-LR, MPI-ESM-MR, MPI-ESM-P, MRI-CGCM3, NorESM1-M. All models are from the r1i1p1 ensemble and forced with the piControl forcing and the abrupt4  $\times \text{CO}_2$  forcing. The time-averaged response 120–150 years after quadrupling  $\text{CO}_2$  is compared to the concurrent pre-industrial control climatology. Simulations specific to pattern scaling are described below.

### Radiative feedbacks

To quantify the radiative response of changing climate variables, the difference in the climate variable between the piControl and abrupt4  $\times \text{CO}_2$  simulations is multiplied by the CESM-CAM5 radiative kernel<sup>42–45</sup>,  $K_a \frac{\delta a}{\delta T_s}$  and  $K_T \frac{\delta T'}{\delta T_s}$ , for the surface albedo and lapse rate feedback, respectively, where  $K_a$  and  $K_T$  are the radiative kernels,  $a$  is surface albedo,  $\delta T'$  is the deviation of the temperature change from vertically uniform warming, and  $\delta T_s$  is the zonal-mean near-surface air temperature change. To obtain the feedback, the radiative flux responses are integrated from the surface to the tropopause, which is determined from temperature using a standard World Meteorological Organization definition<sup>46</sup>.

To further decompose the lapse rate feedback, the 285-K isentrope is used as the boundary between upper and lower regions (Fig. 7). Two modifications are made to the calculation. First, for the upper lapse rate feedback,  $\delta T'$  is defined relative to the temperature change at the (spatially and temporally varying) level where the climatological potential temperature is 285 K, and for the lower lapse rate feedback,  $\delta T'$  is defined relative to the surface temperature change. Second, the vertical integration is performed from the 285-K isentrope to the tropopause for the upper lapse rate feedback and from the surface to the 285-K isentrope for the lower lapse rate feedback. Because the isentrope intersects the surface in the midlatitudes, it effectively separates the high-latitude lower troposphere from both lower latitudes and higher altitudes. It also requires that the lower lapse rate feedback be zero at low latitudes where potential temperature does not drop below 285 K.

Though not the focus of the present study, the Planck feedback,  $\lambda_P$  can be similarly decomposed into a lower portion that warms uniformly with height in accordance with the surface temperature change ( $\delta T|_{T_s}$ ) and an upper portion that warms uniformly in accordance with the temperature change at the 285-K isentrope ( $\delta T|_{\theta=285}$ ). The sum of the lower and upper Planck and

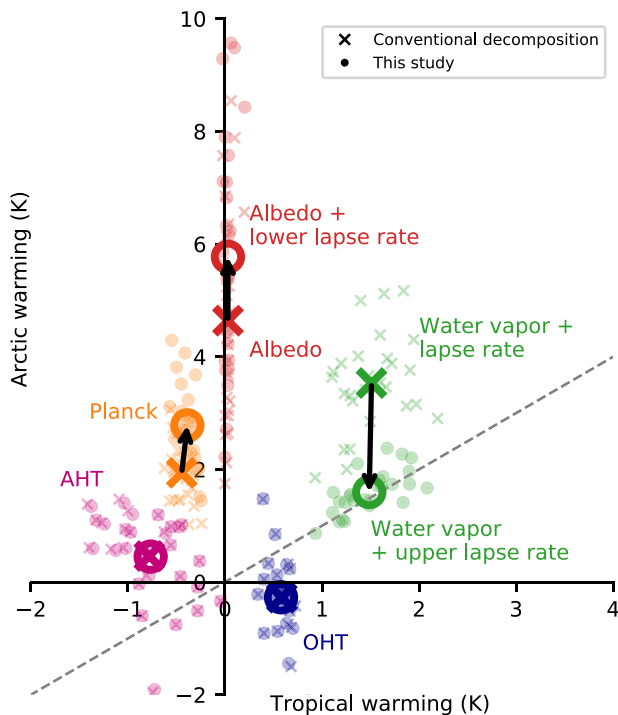


**Fig. 6 Contributions of feedbacks, atmospheric heat transport (AHT), and ocean heat transport (OHT) to Arctic amplification in CMIP5.** Partial surface temperature change for the Arctic ( $60^{\circ}\text{S}$ – $90^{\circ}\text{N}$ ) compared to the tropics ( $30^{\circ}\text{S}$ – $30^{\circ}\text{N}$ ) (e.g., ref. <sup>55</sup>). Crosses are for conventionally defined temperature feedbacks and circles are for temperature feedbacks herein defined.

lapse rate feedbacks by construction equals the sum of the conventionally defined lapse rate feedback and Planck feedbacks,  $\lambda_T$ :

$$\begin{aligned} & \underbrace{\frac{1}{\delta T_s} \int_{p_s}^{p_t} K_T \delta T(p) dp}_{\text{conventional temperature feedback, } \lambda_T} \\ &= \underbrace{\frac{1}{\delta T_s} \int_{p_s}^{p(\theta=285)} K_T \delta T(p) dp}_{\lambda_{T_{\text{lower}}}} + \underbrace{\frac{1}{\delta T_s} \int_{p(\theta=285)}^{p_t} K_T \delta T(p) dp}_{\lambda_{T_{\text{upper}}}} \\ &= \underbrace{\frac{1}{\delta T_s} \int_{p_s}^{p(\theta=285)} K_T \delta T|_{T=T_s} dp}_{\lambda_{p_{\text{lower}}}} + \underbrace{\frac{1}{\delta T_s} \int_{p(\theta=285)}^{p_t} K_T \delta T|_{\theta=285} dp}_{\lambda_{p_{\text{upper}}}} \\ &+ \lambda_{LR_{\text{lower}}} + \lambda_{LR_{\text{upper}}}, \end{aligned} \quad (1)$$

where  $\lambda_{LR_{\text{lower}}} = \lambda_{T_{\text{lower}}} - \lambda_{p_{\text{lower}}}$  and  $\lambda_{LR_{\text{upper}}} = \lambda_{T_{\text{upper}}} - \lambda_{p_{\text{upper}}}$ .

#### Atmospheric energy transport

AET is partitioned into the mean meridional circulation, stationary eddies, and transient eddies <sup>47–50</sup>. The total AET is calculated from the difference between top-of-atmosphere radiative fluxes  $R_T$  and surface radiative and turbulent fluxes  $F_s$ , which includes the latent heat of melting snow,

$$AET = 2\pi a^2 \int_{-\pi/2}^{\phi} [R_T - F_s] \cos \phi' d\phi', \quad (2)$$

where  $a$  is the radius of the Earth,  $\phi$  is the latitude, and brackets indicate zonal mean. The global-mean energy imbalance is removed from the integrand to ensure the transport is zero at the poles.

The mean meridional circulation (MMC) and stationary eddy (STAT) energy transports are calculated explicitly from the meridional wind  $v$  and the moist static energy  $h = c_p T + L_v q + g Z$ , where  $c_p$  is the specific heat of air at constant pressure,  $T$  is the air temperature,  $L_v$  is the latent heat of vaporization of water,  $g$  is the acceleration of gravity, and  $Z$  is the geopotential height. To prevent errors in cases where mass is not conserved in the MMC, we remove the weighted vertical average of the

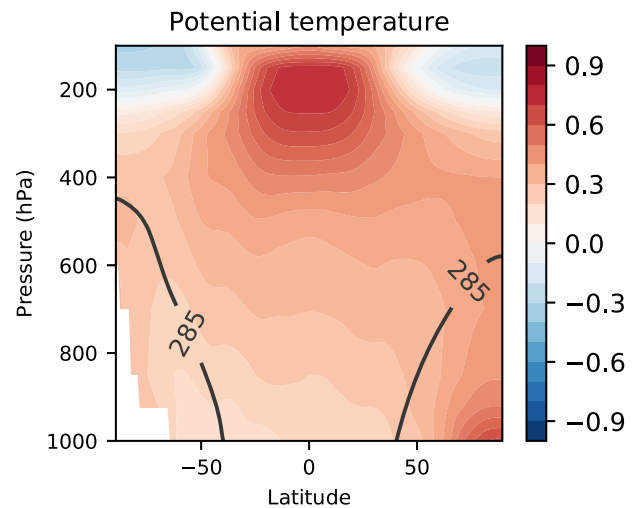


**Fig. 7 Multimodel-mean zonal-mean potential temperature change.** The climatological 285-K potential temperature contour is selected as the boundary between tropical upper-tropospheric warming and high-latitude lower-tropospheric warming.

moist static energy <sup>50</sup>, i.e.,  $\langle \tilde{h} \rangle = [h] - \sum_0^{p_s} [h] dp / \sum_0^{p_s} dp$ .

$$MMC = \frac{2\pi a \cos \phi}{g} \int_0^{p_s} [v] \langle \tilde{h} \rangle dp, \quad (3)$$

$$STAT = \frac{2\pi a \cos \phi}{g} \int_0^{p_s} [v^* h^*] dp, \quad (4)$$

where  $*$  indicates departures from a zonal average. The dry and moist components of the MMC and STAT energy transports can be calculated explicitly by using either the dry static energy ( $c_p T + gZ$ ) or the latent energy ( $L_v q$ ) only in the above equations.

To obtain the dry and moist components of the transient eddy energy transport, it is first necessary to compute the total latent energy transport and dry static energy transport

$$AET_{\text{latent}} = 2\pi a^2 \int_{-\pi/2}^{\phi} L_v [E - P] \cos \phi d\phi, \quad (5)$$

$$AET_{\text{dry}} = AET - AET_{\text{latent}}, \quad (6)$$

where  $E$  is evaporation and  $P$  is precipitation. As in Eq. (2), the global-mean latent energy imbalance must be removed from the integrand of Eq. (5). Finally, transient eddy (TRANS) energy transport and its dry and moist components are calculated as a residual

$$TRANS = AET - (MMC + STAT), \quad (7)$$

$$TRANS_{\text{latent}} = AET_{\text{latent}} - (MMC_{\text{latent}} + STAT_{\text{latent}}), \quad (8)$$

$$TRANS_{\text{dry}} = AET_{\text{dry}} - (MMC_{\text{dry}} + STAT_{\text{dry}}). \quad (9)$$

All calculations are performed on monthly climatologies, and the change in energy transport is the difference between the piControl and abrupt4xCO<sub>2</sub> simulations.

#### CESM pattern scaling

From the empirical observation that the pattern of the forced response to greenhouse warming in climate models is proportional to the global-mean temperature <sup>51,52</sup>, Blackport et al. <sup>20</sup> generalized pattern scaling to multiple climate variables, and we use, as in that study, tropical ( $0$ – $40^{\circ}\text{N}$ ) sea surface temperature ( $T_I$ ) and Arctic sea ice loss ( $I$ ) as the scaling variables. The response pattern of some variable  $Z$  can be decomposed as

$$\delta Z_m = \frac{\partial Z}{\partial I} \bigg|_{T_I} \delta I_m + \frac{\partial Z}{\partial T_I} \bigg|_I \delta T_{I,m}, \quad (10)$$

where  $m$  indicates one of the following RCP8.5 or reduced-albedo experiments. The forced pattern of response to sea ice loss is the difference between the last 340 years of a 540 year-long simulation where

the albedo of sea ice, snow on sea ice, and sea ice underneath melt ponds is reduced globally via the Delta-Eddington tuning parameter<sup>53</sup> (albedo forcing) and the last 435 years of a 735 year-long simulation with perennial year 2000 radiative forcing. Both simulations are from the Community Earth System Model (CESM1-CAM5). The response to RCP8.5 forcing is the difference in the 40-member mean of the Community Earth System Model Large Ensemble (CESM LE)<sup>54</sup> between two epochs (2057–2066 and 2027–2036) chosen such that they approximately represent the same amount of sea ice loss as in the albedo forcing simulations in DJF. For a given season, we use the two response patterns and invert Eq. (10), solving for the sensitivities  $\frac{\partial Z}{\partial T}|_{T_1}$  and  $\frac{\partial Z}{\partial T}|_{T_2}$  that characterize that model. These sensitivities give the patterns of response that scale with tropical warming and with sea ice loss, respectively.

To compute the lapse rate feedback as presented in Fig. 1, we use the following response patterns for atmospheric temperature  $T$ :

- temperature response for RCP8.5,  $\delta T_{\text{RCP8.5}}$
- temperature response for albedo forcing,  $\delta T_{\text{albedo}}$
- the part of the temperature response that scales with low-latitude warming,  $\frac{\partial T}{\partial T}|_{T_1}$ , and
- the part of the temperature response that scales with sea ice loss,  $\frac{\partial T}{\partial T}|_{T_2}$ .

The scaling parameters in (c) are 1.17, 1.15, 1.16, and 1.18 (°C) for DJF, MAM, JJA, and SON, respectively. The scaling parameters in (d) are  $-2.27$ ,  $-1.27$ ,  $-2.32$ , and  $-3.47$  ( $10^6 \text{ km}^2$ ) for DJF, MAM, JJA, and SON, respectively. The atmospheric temperature response patterns are calculated for each season, and a lapse rate feedback is then calculated from each response using the radiative kernel method described above. Hence, the lapse rate feedbacks for the partial temperature response patterns sum to the total lapse rate feedback for the RCP8.5 forcing. The residual of the decomposition is shown in Fig. S6.

## DATA AVAILABILITY

The model output that support the findings of this study are available from the Program for Climate Model Diagnosis and Intercomparison (PCMDI) archive, <https://esgf-node.llnl.gov/projects/cmip5/>.

## CODE AVAILABILITY

Computer code used to generate results is available upon request.

Received: 25 March 2020; Accepted: 15 September 2020;

Published online: 22 October 2020

## REFERENCES

1. Hansen, J. et al. in *Climate Processes and Climate Sensitivity*, (eds. Hansen, J. E. & Takahashi, T.) AGU Geophysical Monograph 29, Maurice Ewing, Vol. 5, 130–163 (American Geophysical Union, Washington, DC, 1984).
2. Colman, R. A comparison of climate feedbacks in general circulation models. *Clim. Dynam.* **20**, 865–873 (2003).
3. Bony, S. et al. How well do we understand and evaluate climate change feedback processes? *J. Clim.* **19**, 3445–3482 (2006).
4. Manabe, S. & Wetherald, R. T. The effects of doubling the  $\text{CO}_2$  concentration on the climate of a general circulation model. *J. Atmos. Sci.* **32**, 3–15 (1975).
5. Bintanja, R., van der Linden, E. C. & Hazelger, W. Boundary layer stability and Arctic climate change: a feedback study using EC-Earth. *Clim. Dynam.* **39**, 2659–2673 (2012).
6. Feldl, N. & Roe, G. H. The nonlinear and nonlocal nature of climate feedbacks. *J. Clim.* **26**, 8289–8304 (2013).
7. Pithan, F. & Mauritsen, T. Arctic amplification dominated by temperature feedbacks in contemporary climate models. *Nat. Geosci.* **7**, 181–184 (2014).
8. Graversen, R. G., Langen, P. L. & Mauritsen, T. Polar amplification in CCSM4: contributions from the lapse rate and surface albedo feedbacks. *J. Clim.* **27**, 4433–4450 (2014).
9. Payne, A. E., Jansen, M. F. & Cronin, T. W. Conceptual model analysis of the influence of temperature feedbacks on polar amplification. *Geophys. Res. Lett.* **42**, 9561–9570 (2015).
10. Holland, M. M., Serreze, M. C. & Stroeve, J. The sea ice mass budget of the Arctic and its future change as simulated by coupled climate models. *Clim. Dynam.* **34**, 185–200 (2010).
11. Stroeve, J. & Notz, D. Changing state of Arctic sea ice across all seasons. *Environ. Res. Lett.* **13**, 103001 (2018).
12. Petty, A. A., Holland, M. M., Bailey, D. A. & Kurtz, N. T. Warm Arctic, increased winter sea ice growth? *Geophys. Res. Lett.* **45**, 12,922–12,930 (2018).
13. Manabe, S. & Stouffer, R. J. Sensitivity of a global climate model to an increase of  $\text{CO}_2$  concentration in the atmosphere. *J. Geophys. Res.* **85**, 5529–5554 (1980).
14. Screen, J. A. & Simmonds, I. Increasing fall-winter energy loss from the Arctic Ocean and its role in Arctic temperature amplification. *Geophys. Res. Lett.* **37**, L16707 (2010).
15. Dai, A., Luo, D., Song, M. & Liu, J. Arctic amplification is caused by sea-ice loss under increasing  $\text{CO}_2$ . *Nat. Commun.* **10**, 121 (2019).
16. Deser, C., Tomas, R. A. & Sun, L. The role of ocean-atmosphere coupling in the zonal-mean atmospheric response to Arctic sea ice loss. *J. Clim.* **28**, 2168–2186 (2015).
17. Blackport, R. & Kushner, P. J. The transient and equilibrium climate response to rapid summertime sea ice loss in CCSM4. *J. Clim.* **29**, 401–417 (2016).
18. Oudar, T. et al. Respective roles of direct GHG radiative forcing and induced Arctic sea ice loss on the Northern Hemisphere atmospheric circulation. *Clim. Dynam.* **49**, 3693–3713 (2017).
19. McCusker, K. E. et al. Remarkable separability of circulation response to Arctic sea ice loss and greenhouse gas forcing. *Geophys. Res. Lett.* **44**, 7955–7964 (2017).
20. Blackport, R. & Kushner, P. J. Isolating the atmospheric circulation response to Arctic sea ice loss in the coupled climate system. *J. Clim.* **30**, 2163–2185 (2017).
21. Smith, D. M. et al. Atmospheric response to Arctic and Antarctic sea ice: the importance of ocean-atmosphere coupling and the background state. *J. Clim.* **30**, 4547–4565 (2017).
22. Screen, J. A., Deser, C. & Simmonds, I. Local and remote controls on observed Arctic warming. *Geophys. Res. Lett.* **39**, L10709 (2012).
23. Laliberté, F. & Kushner, P. J. Isentropic constraints by midlatitude surface warming on the Arctic midtroposphere. *Geophys. Res. Lett.* **40**, 606–611 (2013).
24. Fajber, R., Kushner, P. J. & Laliberté, F. Influence of midlatitude surface thermal anomalies on the polar midtroposphere in an idealized moist model. *J. Atmos. Sci.* **75**, 1089–1104 (2018).
25. Feldl, N., Anderson, B. T. & Bordini, S. Atmospheric eddies mediate lapse rate feedback and Arctic amplification. *J. Clim.* **30**, 9213–9224 (2017).
26. Singh, H. A., Rasch, P. J. & Rose, B. E. J. Increased ocean heat convergence into the high latitudes with  $\text{CO}_2$  doubling enhances polar-amplified warming. *Geophys. Res. Lett.* **44**, 10,583–10,591 (2017).
27. Po-Chedley, S. et al. Sources of intermodel spread in the lapse rate and water vapor feedbacks. *J. Clim.* **31**, 3187–3206 (2018).
28. Yoshimori, M., Abe-Ouchi, A. & Lainé, A. The role of atmospheric heat transport and regional feedbacks in the Arctic warming at equilibrium. *Clim. Dynam.* **49**, 3457–3472 (2017).
29. Stuecker, M. F. et al. Polar amplification dominated by local forcing and feedbacks. *Nat. Clim. Change* **8**, 1076–1081 (2018).
30. Cronin, T. W. & Jansen, M. F. Analytic radiative-advection equilibrium as a model for high-latitude climate. *Geophys. Res. Lett.* **43**, 449–457 (2016).
31. Hay, S., Kushner, P. J., Blackport, R. & McCusker, K. E. On the relative robustness of the climate response to high-latitude and low-latitude warming. *Geophys. Res. Lett.* **45**, 6232–6241 (2018).
32. Feldl, N., Bordini, S. & Merlis, T. M. Coupled high-latitude climate feedbacks and their impact on atmospheric heat transport. *J. Clim.* **30**, 189–201 (2017).
33. Armour, K. C., Marshall, J., Scott, J. R., Donohoe, A. & Newsom, E. R. Southern Ocean warming delayed by circumpolar upwelling and equatorward transport. *Nat. Geosci.* **9**, 549–554 (2016).
34. Rose, B. E. J. & Rencurrel, M. C. The vertical structure of tropospheric water vapor: comparing radiative and ocean-driven climate changes. *J. Clim.* **29**, 4251–4268 (2016).
35. Colman, R. Seasonal contributions to climate feedbacks. *Clim. Dynam.* **20**, 825–841 (2003).
36. Crook, J. A., Forster, P. M. & Stuber, N. Spatial patterns of modeled climate feedback and contributions to temperature response and polar amplification. *J. Clim.* **24**, 3575–3592 (2011).
37. Bintanja, R. & Selten, F. M. Future increases in Arctic precipitation linked to local evaporation and sea-ice retreat. *Nature* **509**, 479–482 (2014).
38. Singh, H. K. A., Bitz, C. M., Donohoe, A. & Rasch, P. J. A source-receptor perspective on the polar hydrologic cycle: sources, seasonality, and Arctic-Antarctic parity in the hydrologic cycle response to  $\text{CO}_2$  doubling. *J. Clim.* **30**, 9999–10017 (2017).
39. Cesspi, P. & Gregory, J. M. Relationship of tropospheric stability to climate sensitivity and Earth's observed radiation budget. *Proc. Nat. Acad. Sci. USA* **114**, 13126–13131 (2017).
40. Andrews, T. & Webb, M. J. The dependence of global cloud and lapse rate feedbacks on the spatial structure of tropical Pacific warming. *J. Clim.* **31**, 641–654 (2018).
41. Taylor, K. E., Stouffer, R. J. & Meehl, G. A. An overview of CMIP5 and the experiment design. *Bull. Am. Meteorol. Soc.* **93**, 485–498 (2012).
42. Soden, B. J. & Held, I. M. An assessment of climate feedbacks in coupled ocean-atmosphere models. *J. Clim.* **19**, 3354–3360 (2006).

43. Soden, B. J. et al. Quantifying climate feedbacks using radiative kernels. *J. Clim.* **21**, 3504–3520 (2008).

44. Shell, K. M., Kiehl, J. T. & Shields, C. A. Using the radiative kernel technique to calculate climate feedbacks in NCAR's Community Atmospheric Model. *J. Clim.* **21**, 2269–2282 (2008).

45. Pendergrass, A. G., Conley, A. & Vitt, F. M. Surface and top-of-atmosphere radiative feedback kernels for CESM-CAM5. *Earth Syst. Sci. Data* **10**, 317–324 (2018).

46. Reichler, T., Dameris, M. & Sausen, R. Determining the tropopause height from gridded data. *Geophys. Res. Lett.* **30**, 2042 (2003).

47. Peixoto, J. P. & Oort, A. H. *Physics of Climate* (Springer, New York, 1992).

48. Trenberth, K. E. & Caron, J. M. Estimates of meridional atmosphere and ocean heat transports. *J. Clim.* **14**, 3433–3443 (2001).

49. Trenberth, K. E. & Stepaniak, D. P. Covariability of components of poleward atmospheric energy transports on seasonal and interannual timescales. *J. Clim.* **16**, 3691–3705 (2003).

50. Donohoe, A., Armour, K. C., Roe, G. H., Battisti, D. S. & Hahn, L. The partitioning of meridional heat transport from the Last Glacial Maximum to CO<sub>2</sub> quadrupling in coupled climate models. *J. Clim.* **33**, 4141–4165 (2020).

51. Santer, B. D., Wigley, T. M. L., Schelsinger, M. E. & Mitchell, J. F. B. *Developing Climate Scenarios from Equilibrium GCM Results*. Tech. rep., Max-Planck-Institut für Meteorologie, Hamburg (1990).

52. Tebaldi, C. & Arblaster, J. M. Pattern scaling: its strengths and limitations, and an update on the latest model simulations. *Clim. Change* **122**, 459–471 (2014).

53. Briegleb, B. P. & Light, B. *A Delta-Eddington Multiple Scattering Parameterization for Solar Radiation in the Sea Ice Component of the Community Climate System Model*. Tech. rep., Boulder, CO (2007).

54. Kay, J. E. et al. The Community Earth System Model (CESM) large ensemble project: a community resource for studying climate change in the presence of internal climate variability. *Bull. Am. Meteorol. Soc.* **96**, 1333–1349 (2015).

55. Goosse, H. et al. Quantifying climate feedbacks in polar regions. *Nat. Commun.* **9**, 1–13 (2018).

## ACKNOWLEDGEMENTS

N.F. was supported by NSF grant AGS-1753034. Work performed by S.P.-C. at Lawrence Livermore National Laboratory (LLNL) was under the auspices of the U.S. Department of Energy under Contract DE-AC52-07NA27344 with funding from the National Science Foundation (AGS-1624881) and LLNL LDRD 18-ERD-054. S.H. was supported by the Natural Sciences and Engineering Research Council of Canada Discovery Grant program and U.S. Department of Energy Grant DE-SC0019407.

## AUTHOR CONTRIBUTIONS

N.F. conceived the research. N.F. and S.P. designed and performed analysis. S.H. performed pattern-scaling research. N.F., S.P., H.K.A.S., P.J.K., and S.H. interpreted data. N.F. drafted the manuscript, and S.P., H.K.A.S., P.J.K., and S.H. revised it critically. All authors approved the final manuscript.

## COMPETING INTERESTS

The authors declare no competing interests.

## ADDITIONAL INFORMATION

**Supplementary information** is available for this paper at <https://doi.org/10.1038/s41612-020-00146-7>.

**Correspondence** and requests for materials should be addressed to N.F.

**Reprints and permission information** is available at <http://www.nature.com/reprints>

**Publisher's note** Springer Nature remains neutral with regard to jurisdictional claims in published maps and institutional affiliations.



**Open Access** This article is licensed under a Creative Commons Attribution 4.0 International License, which permits use, sharing, adaptation, distribution and reproduction in any medium or format, as long as you give appropriate credit to the original author(s) and the source, provide a link to the Creative Commons license, and indicate if changes were made. The images or other third party material in this article are included in the article's Creative Commons license, unless indicated otherwise in a credit line to the material. If material is not included in the article's Creative Commons license and your intended use is not permitted by statutory regulation or exceeds the permitted use, you will need to obtain permission directly from the copyright holder. To view a copy of this license, visit <http://creativecommons.org/licenses/by/4.0/>.

© The Author(s) 2020